

21. AIMAll, Version 14.11.23; aim.tkgristmill.com.
22. R. F. W. Bader, *Chem. Rev.* **91**, 893–928 (1991).
23. W. V. F. Brooks, T. S. Cameron, S. Parsons, J. Passmore, M. J. Schriver, *Inorg. Chem.* **33**, 6230–6241 (1994).
24. Z. Chen, C. S. Wannere, C. Corminboeuf, R. Puchta, P. Schleyer, *Chem. Rev.* **105**, 3842–3888 (2005).
25. A. Stanger, *J. Org. Chem.* **71**, 883–893 (2006).
26. C. Foroutan-Nejad, *J. Phys. Chem. A* **115**, 12555–12560 (2011).
27. See supplementary materials on Science Online.
28. F. Weinhold, R. A. Klein, *Mol. Phys.* **110**, 565–579 (2012).
29. H. Hamaguchi, M. Tasumi, M. Yoshifuji, N. Inamoto, *J. Am. Chem. Soc.* **106**, 508–509 (1984).
30. J. Pople, W. G. Schneider, H. J. Bernstein, *High Resolution Nuclear Magnetic Resonance* (McGraw-Hill, New York, 1959).
31. W. H. Hersh, *J. Chem. Educ.* **74**, 1485 (1997).
32. F. Neese, *ORCA—an Ab Initio, Density Functional and Semiempirical Program Package*, Version 3.0.1 (University of Bonn, 2013).
33. E. D. Glendening, J. K. Badenhoop, F. Weinhold, *J. Comput. Chem.* **19**, 628–646 (1998).
34. NBO 5.0 (Theoretical Chemistry Institute, University of Wisconsin, 2001).
35. NBOView 2.0: NBO Orbital Graphics Plotter (University of Wisconsin, 2013).

ACKNOWLEDGMENTS

This material is based on work supported by NSF grant CHE-1362118.

SUPPLEMENTARY MATERIALS

www.sciencemag.org/content/348/6238/1001/suppl/DC1
Materials and Methods
Figs. S1 to S13
Tables S1 to S15
References (36–56)

1 March 2015; accepted 5 May 2015
10.1126/science.aab0204

SHAPE MEMORY ALLOYS

Ultralow-fatigue shape memory alloy films

Christoph Chluba,¹ Wenwei Ge,² Rodrigo Lima de Miranda,¹ Julian Strobel,¹ Lorenz Kienle,¹ Eckhard Quandt,^{1*} Manfred Wuttig^{2*}

Functional shape memory alloys need to operate reversibly and repeatedly. Quantitative measures of reversibility include the relative volume change of the participating phases and compatibility matrices for twinning. But no similar argument is known for repeatability. This is especially crucial for many future applications, such as artificial heart valves or elastocaloric cooling, in which more than 10 million transformation cycles will be required. We report on the discovery of an ultralow-fatigue shape memory alloy film system based on TiNiCu that allows at least 10 million transformation cycles. We found that these films contain Ti₂Cu precipitates embedded in the base alloy that serve as sentinels to ensure complete and reproducible transformation in the course of each memory cycle.

Shape memory alloys (SMAs) are attractive because of their distinct properties. The shape memory effect (1) is the basis in many modern solid-state actuators (2). Medical implants such as self-expanding stents (3) or orthodontic arch wires (4) take advantage of the superelasticity (1). This property also finds application in the emerging field of elastocaloric solid-state refrigerators (5). The basic principle of both features is the reversible martensite-austenite transformation, which is temperature-driven in the case of the shape memory effect and stress-driven in the case of the superelasticity. The corresponding large work output of SMAs is a consequence of a first-order structural phase transformation featuring a large eigenstrain and substantial enthalpy of transformation (6, 7). In apparent contradiction to its first-order characteristic, the property-controlling phase transformation of SMAs is reversible because the transforming phases are elastically compatible, meaning that the structural distortions arising from the transformation do not exceed the limits of reversibility (8). Nevertheless, a limiting factor for any high-cycle application of either

property is fatigue, both the integrity of the material (structural fatigue) as well as the change of their functional properties and their reversibility (functional fatigue). A general understanding of how often the transformation can be executed in polycrystals—its fatigue characteristics—is lacking, even though it currently constitutes the major obstacle to the implementation of the new technologies (9).

The most prominent SMAs are based on titanium-nickel, for which an equiatomic composition of the shape memory effect was uncovered in 1963 (10). The specific combination of their large effect sizes, tunability of the transformation temperatures by partial substitution of Ni or Ti with other elements (such as Cu, Pd, Pt, Co, Fe, and Hf), good mechanical properties, and excellent biocompatibility in case of binary TiNi (11) results in these alloys being the first choice for most solid-state shape memory and superelasticity applications. Despite the almost ubiquitous use of binary TiNi for superelastic implants (12), these alloys show a dramatic fatigue upon full cycling of the stress-induced martensitic transformation. Even for the first cycles, a change in the transformation temperature (13), a decrease of the superelastic plateau strain, and an accumulation of residual martensite are observed (14). Different fatigue investigations have revealed the fatigue endurance limit (maximum strain amplitude for run-out at 10 million cycles) for bulk superelastic TiNi to be between 0.4 and 0.6%, which is almost independent from the mean strain (3, 13). For example, the superelastic fatigue life in TiNi and TiNiCu wires by using a less-demanding rotary bending fatigue tester only reached 1 million cycles if the maximum stress at the outer surface was smaller than 0.8% (15). This behavior implies that only partial transformations can be used for any high-cycle applications,

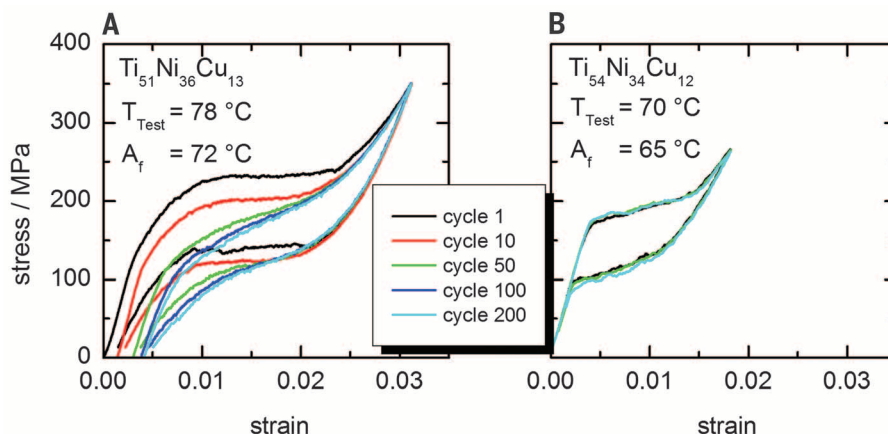


Fig. 1. Evolution of fatigue in SMA films. (A and B) Fatigue stress-strain curves of tensile fatigue tests performed up to 200 cycles at test temperatures (T_{Test}) larger than austenite finish temperature (A_f) noted in (A) and (B). Fatigue characteristics of near-equiatomic Ti₅₁Ni₃₆Cu₁₃ (sample 1) films with strong fatigue behavior and mechanically stable Ti-rich Ti₅₄Ni₃₄Cu₁₂ (sample 2) films are shown.

¹Institute for Materials Science, Faculty of Engineering, University of Kiel, Kiel, Germany. ²Department of Materials Science and Engineering, University of Maryland, College Park, MD, USA.

*Corresponding author. E-mail: eq@tfi.uni-kiel.de (E.Q.); wuttig@umd.edu (M.W.)

which is considered to be the major drawback of elastocaloric materials besides the observed pronounced functional fatigue (16). The behavior is related to the incompleteness of the transformation upon cycling (17), resulting in surface roughness, which is believed to be the origin of crack formation and subsequent mechanical failure of the material.

The obstacles described above demonstrate the connection between reversibility (functional fatigue) with structural fatigue. Essential for the reversibility are both the compatibility of the martensite-austenite and the twin/twin interfaces. The former and latter are perfect when the compatibility triplet—which consists of the middle eigenvalue of the stretch matrix measuring the relative volume change of the transforming phases, λ , and the two cofactors measuring the mutual compatibility of type I and II twins, CCI and CCII (18)—attains the values (1,0,0). Combinatorial techniques were used to identify compositions fulfilling the first condition in the systems Ni-Ti-Cu and Ni-Ti-Pd (7). In $\text{Zn}_{45}\text{Au}_{30}\text{Cu}_{25}$ polycrystals, all compatibility conditions are close to their ideal values. Hence, the alloy displayed superior functional stability. This translated to the observation of a small decrease of the latent heat of $\approx 10\%$ that persisted up to 1.6×10^4 transformation cycles (19).

Additional interest in shape memory materials arises from the development of thin-film technology—which has led to miniaturized applications (20) such as microelectromechanical sys-

tem (MEMS) actuators (21)—as medical implants and for elastocaloric cooling (22). Besides miniaturization, these materials and related devices benefit from the high surface-to-volume ratio of thin-film SMAs and high specific work and power output owing to their enhanced frequency capabilities. In addition, free-standing thin-film materials, fabricated by use of a special sacrificial layer technique (23), exhibit improved mechanical and fatigue properties because of the absence of inclusions (24).

This study was undertaken so as to better understand the reversibility of the martensitic transformation in TiNiCu alloys with Cu substitution of 12.5 ± 0.5 atomic % on Ni positions because they are known to have lower functional fatigue as compared with that of binary TiNi (22). We conducted experiments on thin films so as to minimize the influence of inclusions. TiNi-based devices are commonly made of near-equiatomic compositions (between the Ti- and the Ni-site) in order to minimize the fraction of precipitates and thereby maximize the fraction of phase-transforming material. We intentionally examined a Ti-rich composition in comparison with a near-equiatomic alloy in order to investigate the influence of two types of Ti-rich precipitates, Ti_2Ni and Ti_2Cu , on the functional fatigue. Magnetron-sputtered equiatomic $\text{Ti}_{51}\text{Ni}_{36}\text{Cu}_{13}$ (sample 1) and Ti-rich $\text{Ti}_{54}\text{Ni}_{34}\text{Cu}_{12}$ (sample 2) free-standing samples (25) show an austenite finish temperature (A_f) of $\sim 62^\circ\text{C}$ (fig. S1). We investigated both samples' mechanical (Fig. 1)

and thermal (fig. S1) fatigue characteristics (25), their structure before and after deformation cycling, as well as the crystallographic structures above and below A_f by means of synchrotron-based x-ray diffraction (XRD) (25). Additionally, we used high-resolution transmission electron microscopy (HRTEM) to characterize the B2/ Ti_2Cu and B19/ Ti_2Cu interfaces. We found that the presence of Ti_2Cu precipitates and next-to-ideal values of the compatibility triplet increase the fatigue limit of the Ti-rich sample to more than 10^7 full cycles without any degradation in the effect size. This insight allows us to transfer the principle to other phase transformation-controlled materials such as TiNiCuCo thin films (fig. S2).

The fatigue characteristics are different between the two samples within the first 200 cycles: A traditional SMA (sample 1) shows large functional fatigue (Fig. 1A), characterized by accumulation of remanent martensite (Table 1). The transformation is stabilized after 100 cycles, but high-cycle tests revealed an early rupture of this material after several thousand cycles. Increased surface roughness originating from stabilized martensite, which served as crack nucleation sites, is the likely mechanism (26). In contrast, the Ti-rich alloy (sample 2) displayed no measurable fatigue (Fig. 1B). However, as a result of the higher-mass fraction of precipitates (Table 1), the low-fatigue sample 2 showed a reduced superelastic plateau. A similar difference of the fatigue characteristics is found for TiNiCuCo samples. The near-equiatomic sample exhibits distinct fatigue (fig. S2A), whereas the Ti-rich sample displays no fatigue and a reduced superelastic strain (fig. S2B). Most noteworthy, the ultralow fatigue for the Ti-rich samples can be extended to 10 million cycles (Fig. 2 and fig. S3).

A comparison of the results of the diffraction experiments to the fatigue data (Figs. 1 and 2)

Table 1. Refinement of mass fraction (m) and lattice parameters (a , b , and c) of the phases identified before and after 200 deformation cycles for the high- and low-fatigue $\text{Ti}_{51}\text{Ni}_{36}\text{Cu}_{13}$ and $\text{Ti}_{54}\text{Ni}_{34}\text{Cu}_{12}$. The Rietveld mass fraction uncertainties are much smaller than expected (31), which explains the apparent inconsistencies of the Ti_2Cu mass fractions at 22°C and 87°C . Numbers in parentheses are rounded.

		At 22°C		At 87°C	
		Before cycling	After cycling	Before cycling	After cycling
$\text{Ti}_{51}\text{Ni}_{36}\text{Cu}_{13}$, sample 1: Identified phases					
B2 ($Pm\bar{3}m$)	m [%]			81.35(2)	74.77(2)
	a [Å]			3.036050(5)	3.03691(1)
	m [%]	93.484(8)	92.414(8)	12.31(7)	18.52(6)
B19 ($Pmma$)	a	$a = 4.24731(5)$	$a = 4.24864(6)$	$a = 4.2546(5)$	$a = 4.2668(5)$
	b	$b = 2.89549(5)$	$b = 2.89582(5)$	$b = 2.9028(4)$	$b = 2.9127(4)$
	c	$c = 4.52777(4)$	$c = 4.52669(4)$	$c = 4.5157(4)$	$c = 4.5089(3)$
Ti_2Ni ($Fd\bar{3}m$)	m [%]	6.52(5)	7.59(4)	6.34(5)	6.71(4)
	a [Å]	11.3421(4)	11.3467(3)	11.3519(2)	11.3575(2)
$\text{Ti}_{54}\text{Ni}_{34}\text{Cu}_{12}$, sample 2: Identified phases					
B2 ($Pm\bar{3}m$)	m [%]			67.89(3)	70.30(3)
	a [Å]			3.038542(4)	3.038653(4)
	m [%]	71.45(3)	73.65(2)		
B19 ($Pmma$)	a	$a = 4.25653(7)$	$a = 4.25486(7)$		
	b	$b = 2.90113(6)$	$b = 2.90214(6)$		
	c	$c = 4.51964(7)$	$c = 4.52099(7)$		
Ti_2Ni ($Fd\bar{3}m$)	m [%]	22.84(5)	19.15(4)	24.20(5)	20.33(5)
	a [Å]	11.33396(5)	11.33495(6)	11.33981(3)	11.34131(4)
	m [%]	5.71(4)	7.21(4)	7.91(3)	9.37(4)
Ti_2Cu ($I4/mmm$)	$a = b$	$a = b =$	$a = b =$	$a = b =$	$a = b =$
	c	$c = 2.95131(3)$	$c = 2.95100(3)$	$c = 2.95556(2)$	$c = 2.95549(2)$
		$c = 10.4993(2)$	$c = 10.5015(2)$	$c = 10.49195(9)$	$c = 10.49451(9)$

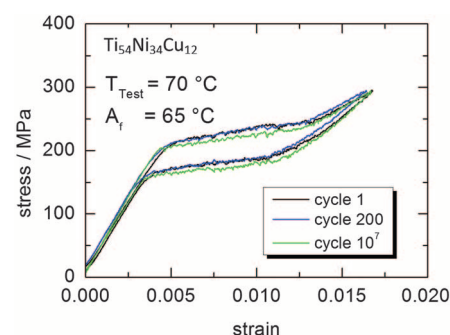


Fig. 2. Ultralow fatigue in SMA films. Ultralow fatigue of the Ti-rich sample 2 demonstrated by next-to-identical 1st, 200th, and 10^7 th superelastic transformation cycles. The testing temperature (T_{Test}) was 70°C with an austenite-finish temperature (A_f) of 65°C . The high-cycle fatigue at 70°C was measured with a special fatigue test device, consisting of a load cell, a temperature chamber, and a solenoid as actuator. The fatigue test is conducted force-controlled at a frequency of 20 Hz (fig. S4). Cycle 1 to 200 and cycle 10^7 was measured by using a conventional tensile test device (25).

shows that the Ti-rich sample 2 with ultralow fatigue contains Ti_2Cu precipitates, which are not present in the near-equiatomic sample 1 film

(figs. S5 and S6). Both samples contain B2, B19, and Ti_2Ni phases with phase contents (Table 1) and strain distributions (table S1) determined by

means of Rietveld refinements that included grain size (table S2, A and B) (27) as well as anisotropic strain parameters (28). The incomplete temperature-induced $\text{B2} \leftrightarrow \text{B19}$ transformation in sample 1 indicated stabilized martensite in the austenite phase. The presence or absence of Ti_2Cu phase appears to control the transformation and fatigue characteristics of the two samples. We reason that the potential epitaxy of the phase pairs $\text{B2}/\text{Ti}_2\text{Cu}$ and $\text{B19}/\text{Ti}_2\text{Cu}$ is responsible for the almost complete reversibility of the stress-strain curves and identified the relevant misfit strains (Fig. 3 and table S3) along with the corresponding Rietveld strain parameters (S_{hkl}) (table S1) (28) for these interfaces. Taking the strain parameters into consideration improves the refinement considerably (table S4A). The small misfits of the transforming phases' lattice parameters with Ti_2Cu in the low-fatigue sample 2 (Fig. 3) suggest that B19 and B2 are epitaxially related to Ti_2Cu and to each other. The Rietveld strain parameters (table S1) support the epitaxy because the symmetry is identical to that of the anisotropic broadening of diffraction peaks associated with epitaxial strains. TEM diffraction patterns also suggest epitaxy, taken at the $\text{B2}/\text{Ti}_2\text{Cu}$ and $\text{B19}/\text{Ti}_2\text{Cu}$ interfaces (Fig. 4), as also confirmed with HRTEM observations (fig. S8). In contrast, the Ti_2Ni precipitates display larger misfits and small values of the Rietveld strain parameters (fig. S9 and tables S1 and S3). This demonstrates incoherent precipitation in the B2 and B19 phase, respectively.

The refined x-ray and TEM diffraction data suggest the following scenario leading to the low-fatigue state in Ti-rich sample 2. Ti_2Cu coherently

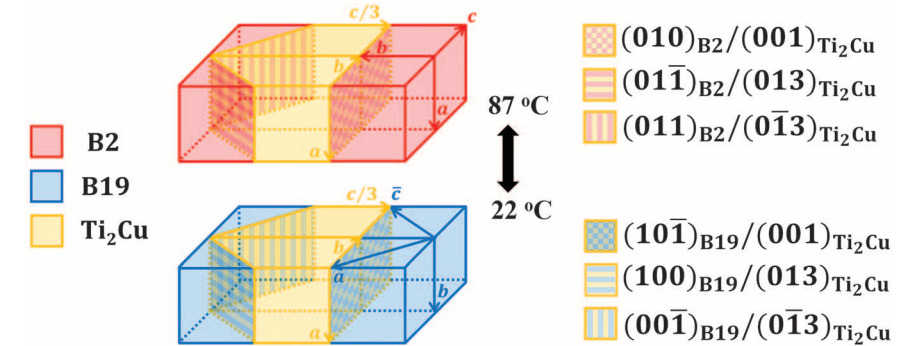
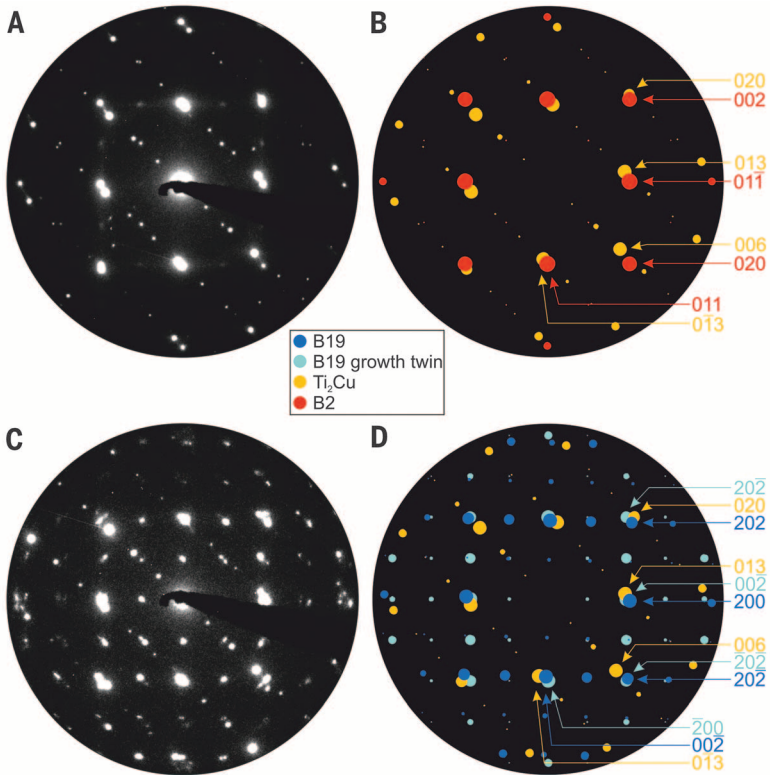


Fig. 3. Dual epitaxies in $\text{Ti}_{54}\text{Ni}_{34}\text{Cu}_{12}$ films. $\text{B2} \leftrightarrow \text{Ti}_2\text{Cu} \leftrightarrow \text{B19}$ epitaxies in $\text{Ti}_{54}\text{Ni}_{34}\text{Cu}_{12}$ film (sample 2). Color coding is shown on the left. The smallest misfit strains, calculated on the basis of the lattice parameters (Table 1), are $\epsilon_{\parallel}[(010)_{\text{B2}}/(001)_{\text{Ti}_2\text{Cu}}] = \frac{2c(\text{B2})}{2b(\text{Ti}_2\text{Cu})} - 1 = 2.80\%$, $\epsilon_{\perp}[(010)_{\text{B2}}/(001)_{\text{Ti}_2\text{Cu}}] = \frac{a(\text{B2})}{a(\text{Ti}_2\text{Cu})} - 1 = 2.80\%$, $\epsilon_{\parallel}[(100)_{\text{B19}}/(013)_{\text{Ti}_2\text{Cu}}] = \frac{c(\text{B19})}{\sqrt{b^2 + (c/3)^2(\text{Ti}_2\text{Cu})}} - 1 = -1.28\%$, and $\epsilon_{\perp}[(100)_{\text{B2}}/(013)_{\text{Ti}_2\text{Cu}}] = \frac{b(\text{B19})}{a(\text{Ti}_2\text{Cu})} - 1 = -1.70\%$. B19 growth twin epitaxies are shown in fig. S7. Additional misfit strains are given in table S3.

Table 2. Values of the compatibility triplet, middle eigenvalue (λ), and cofactor conditions for type I and II twins (CCI and CCII). These are evaluated by using the lattice parameters extracted from Table 1.

Alloy	a_o (Å)	a (Å)	b (Å)	c (Å)	λ	CCI [10^{-4}]	CCII [10^{-4}]
	B2, 87°C	B19, 22°C					
Ti ₅₁ Ni ₃₆ Cu ₁₃	3.03605	4.24732	2.89549	4.52777	0.9892	2.4542	2.9473
Ti ₅₄ Ni ₃₄ Cu ₁₂	3.03854	4.25654	2.90114	4.51964	0.9905	1.8661	2.2742

Fig. 4. Electron microscopical evidence of dual epitaxies. TEM-generated and simulated diffraction patterns of the $\text{B2}/\text{Ti}_2\text{Cu}$ and $\text{B19}/\text{Ti}_2\text{Cu}$ interfaces. The experimental patterns have been recorded on sample 2, patterns (A) and (C), at an elevated and room temperature, respectively. A HRTEM of the interfacial region is shown in fig. S2. (A) Selected-area electron diffraction (SAED) pattern recorded at the $\text{B2}/\text{Ti}_2\text{Cu}$ interface, zone axes $[100]$. (B) Simulation of the pattern in (A), showing that $020_{\text{Ti}_2\text{Cu}}$ nearly coincides with 002_{B2} . (C) SAED pattern recorded at the $\text{B19}/\text{Ti}_2\text{Cu}$ interface; zone axes are $[100]_{\text{Ti}_2\text{Cu}}$ and $[010]_{\text{B19}}$. (D) Simulation of the pattern in (C) demonstrating near-overlap of the $020_{\text{Ti}_2\text{Cu}}$ and $202_{\text{B19}}/202_{\text{B19twin}}$ diffraction spots. The patterns confirm the proposed epitaxies at high and low temperatures: $(010)_{\text{B2}}/(001)_{\text{Ti}_2\text{Cu}}$, red/yellow in Fig. 3; $(101)_{\text{B19}}/(001)_{\text{Ti}_2\text{Cu}}$, dark blue/yellow in Fig. 3; and $(101)_{\text{B19twin}}/(001)_{\text{Ti}_2\text{Cu}}$, light blue/yellow in fig. S7



and Ti_2Ni incoherently precipitate in the B2 matrix upon cooling from 700°C to 87°C. The B2 matrix transforms completely to B19 upon further cooling to 22°C, aided by the simultaneous Ti_2Cu /B19 epitaxies (Figs. 3 and 4, Table 1, and table S3). The B19/ Ti_2Cu epitaxy provides an internal stress pattern, which stabilizes the B19 phase at low temperatures. During stress cycling, the equivalent epitaxy alternately stabilizes the B2 phase. At each temperature and stress, the transforming phases attain equilibrium by forming a compatible morphology directed by the internal epitaxy-generated stress distribution. Complete transformation is attained at each cycle because the epitaxial stresses are reversible. Hence, we propose that the epitaxially promoted completion of the B2 \leftrightarrow B19 phase transformation creates the low-fatigue state of the $\text{Ti}_{54}\text{Ni}_{34}\text{Cu}_{12}$ films. The Ti_2Cu precipitates act like sentinels, assuring that the B2 \leftrightarrow B19 transformation proceeds toward completion at each cycle. The transformation will return the film to a stress state and morphology that are compatible with the pristine state. The decrease of the anisotropic peak broadening of the epitaxy-effected XRD peaks indicates trainability.

This proposal must be revisited in light of the favorable values of the quantitative compatibility criteria calculated from the lattice parameters of both alloys $\text{Ti}_{57}\text{Ni}_{36}\text{Cu}_{13}$ and $\text{Ti}_{54}\text{Ni}_{34}\text{Cu}_{12}$ (Table 2). These values approach the ideal triplet ($\lambda = 1$, $\text{CCI} = \text{CCII} = 0$) and suggest good reversibility even in polycrystals (29), although they are inferior to those for $\text{Zn}_{45}\text{Au}_{30}\text{Cu}_{25}$ (19). The values for sample 2 are closer to the ideal than those for sample 1, which is in accord with the vastly better fatigue characteristics of sample 2. The question then arises whether this large difference of the fatigue life results from the observed epitaxy or that of the two triplets listed in Table 2. We observe that despite their reversibility, the phase transformations in SMAs are of first order (nucleation- and growth-controlled). We suggest that the epitaxy leads to reversible nucleation, whereas the low cofactors promote reversible near-equilibrium growth so that the combination of both mechanisms yields the observed ultralow fatigue. In the limit of CCI and CCII \rightarrow 0, no energy will be stored in the product phase in the form of twin boundaries. This creates a strongly reproducible, and therefore repeatedly transformable, equilibrium state.

Given the fatigue-controlling importance of the dual epitaxy of Ti_2Cu in TiNiCu -based (SMA) films, it is natural to search for other alloying elements that have the potential to play a similar role. Following this lead, we can assume that structurally related Ti_2Ag precipitates will act very similar to Ti_2Cu . Because TiNiAg SMAs display transformation characteristics comparable with that of TiNiCu (30), they could be promising candidates for biocompatible ultralow fatigue SMA films. Elastocaloric cooling requires bulk materials, which is a difficult but, in principle, solvable challenge. More generally, we expect similar behavior in phase-transforming materials that contain dual-epitaxial precipitates.

REFERENCES AND NOTES

1. K. Otsuka, X. Ren, *Prog. Mater. Sci.* **50**, 511–678 (2005).
2. J. Mohd Jani, M. Leary, A. Subic, M. A. Gibson, *Mater. Des.* **56**, 1078–1113 (2014).
3. T. Duerig, A. Pelton, D. Stöckel, *Mater. Sci. Eng. A* **273–275**, 149–160 (1999).
4. D. W. Raboud, M. G. Faulkner, A. W. Lipsett, *Smart Mater. Struct.* **9**, 684–692 (2000).
5. E. Bonnot, R. Romero, L. Mañosa, E. Vives, A. Planes, *Phys. Rev. Lett.* **100**, 125901 (2008).
6. K. Otsuka, C. M. Wayman, Eds., *Shape Memory Materials* (Cambridge Univ. Press, Cambridge, 1999).
7. J. Cui et al., *Nat. Mater.* **5**, 286–290 (2006).
8. K. Bhattacharya, S. Conti, G. Zanzotto, J. Zimmer, *Nature* **428**, 55–59 (2004).
9. X. Moya, S. Kar-Narayan, N. D. Mathur, *Nat. Mater.* **13**, 439–450 (2014).
10. W. J. Buehler, J. V. Gilfrich, R. C. Wiley, *J. Appl. Phys.* **34**, 1475–1477 (1963).
11. S. A. Shabalovskaya, *Biomed. Mater. Eng.* **12**, 69–109 (2002).
12. N. B. Morgan, *Mater. Sci. Eng. A* **378**, 16–23 (2004).
13. A. R. Pelton, *J. Mater. Eng. Perform.* **20**, 613–617 (2011).
14. G. Eggeler, E. Hornbogen, A. Yawny, A. Heckmann, M. Wagner, *Mater. Sci. Eng. A* **378**, 24–33 (2004).
15. S. Miyazaki, K. Mizukoshi, T. Ueki, T. Sakuma, Y. Liu, *Mater. Sci. Eng. A* **273–275**, 658–663 (1999).
16. E. Hornbogen, *J. Mater. Sci.* **39**, 385–399 (2004).
17. K. Gall, H. J. Maier, *Acta Mater.* **50**, 4643–4657 (2002).
18. R. D. James, Z. Zhang, in *Magnetism and Structure in Functional Materials*, A. Planes, L. Manosa, A. Saxena, Eds. (Springer, New York, 2005), vol. 79.
19. Y. Song, X. Chen, V. Dabade, T. W. Shield, R. D. James, *Nature* **502**, 85–88 (2013).
20. S. Miyazaki, Y. Q. Fu, W. M. Huang, Eds., *Thin Film Shape Memory Alloys* (Cambridge Univ. Press, Cambridge, 2009).
21. K. Bhattacharya, R. D. James, *Science* **307**, 53–54 (2005).
22. C. Bechtold, C. Chluba, R. Lima de Miranda, E. Quandt, *Appl. Phys. Lett.* **101**, 091903 (2012).
23. R. Lima de Miranda, C. Zamponi, E. Quandt, *Adv. Eng. Mater.* **15**, 66–69 (2013).
24. G. Siekmeyer, A. Schüßler, R. de Miranda, E. Quandt, *J. Mater. Eng. Perform.* **23**, 2437–2445 (2014).
25. Materials and methods are available as supplementary materials on Science Online.
26. K. Bhattacharya, *Microstructure of Martensite: Why It Forms and How It Gives Rise to the Shape-Memory Effect* (Oxford Univ. Press, Oxford, 2003).
27. A. C. Larson, R. B. Von Dreele, “General Structure Analysis System (GSAS),” Los Alamos National Laboratory Report LAUR 86-748 (2004).
28. P. Stephens, *J. Appl. Cryst.* **32**, 281–289 (1999).
29. K. Bhattacharya, R. V. Kohn, *Acta Mater.* **44**, 529–542 (1996).
30. C. Zamponi, M. Wuttig, E. Quandt, *Scripta Mater.* **56**, 1075–1077 (2007).
31. H. Scott, *J. Appl. Cryst.* **16**, 159–163 (1983).

ACKNOWLEDGMENTS

The work at the University of Kiel was supported by the Deutsche Forschungsgemeinschaft (DFG) via the Priority Program 1599. L.K. and J.S. appreciate the assistance of V. Duppel (Max Planck Institute for solid state research) for recording the electron diffraction patterns, B. V. Lotsch for enabling electron microscopy, and C. Szillus for TEM sample preparation. The work at the University of Maryland was supported by grant DOE DESC0005448; use of the Advanced Photon Source - Argonne National Laboratory was supported by the U.S. Department of Energy (DOE) Office of Science, under contract DE-AC02-06CH11357. M.W. and W.G. thank P. Zavali for his guidance with the Rietveld refinement and J. Steiner for the compatibility calculations. The synchrotron diffraction data are available from the corresponding author. Other data are available in the main text and the supplementary materials.

SUPPLEMENTARY MATERIALS

www.sciencemag.org/content/348/6238/1004/suppl/DC1
Materials and Methods

Figs. S1 to S9

Tables S1 to S4

Reference (32)

12 September 2014; accepted 14 April 2015
10.1126/science.1261164

MEMORY

Engram cells retain memory under retrograde amnesia

Tomás J. Ryan,^{1,2*} Dheeraj S. Roy,^{1*} Michele Pignatelli,^{1*} Autumn Arons,^{1,2} Susumu Tonegawa^{1,2†}

Memory consolidation is the process by which a newly formed and unstable memory transforms into a stable long-term memory. It is unknown whether the process of memory consolidation occurs exclusively through the stabilization of memory engrams. By using learning-dependent cell labeling, we identified an increase of synaptic strength and dendritic spine density specifically in consolidated memory engram cells. Although these properties are lacking in engram cells under protein synthesis inhibitor-induced amnesia, direct optogenetic activation of these cells results in memory retrieval, and this correlates with retained engram cell-specific connectivity. We propose that a specific pattern of connectivity of engram cells may be crucial for memory information storage and that strengthened synapses in these cells critically contribute to the memory retrieval process.

Memory consolidation is the phenomenon by which a newly formed memory transitions from a fragile state to a stable, long-term state (1–3). The defining feature of consolidation is a finite time window that begins immediately after learning,

during which a memory is susceptible to disruptions, such as protein synthesis inhibition (4–6), resulting in retrograde amnesia. The stabilization of synaptic potentiation is the dominant cellular model of memory consolidation (7–10) because protein synthesis inhibitors disrupt late-phase

Ultralow-fatigue shape memory alloy films

Christoph Chluba, Wenwei Ge, Rodrigo Lima de Miranda, Julian Strobel, Lorenz Kienle, Eckhard Quandt and Manfred Wuttig

Science **348** (6238), 1004-1007.

DOI: 10.1126/science.1261164

Memory alloys that avoid exhaustion

Shape memory alloys can pop back into shape after being deformed. However, often these alloys cannot cope with a large number of deformation cycles. Chluba *et al.* find an alloy that avoids this pitfall, deforming 10 million times with very little fatigue (see the Perspective by James). Such low-fatigue materials could be useful in a plethora of future applications ranging from refrigerators to artificial heart valves.

Science, this issue p. 1004; see also p. 968

ARTICLE TOOLS

<http://science.sciencemag.org/content/348/6238/1004>

SUPPLEMENTARY MATERIALS

<http://science.sciencemag.org/content/suppl/2015/05/27/348.6238.1004.DC1>

RELATED CONTENT

<http://science.sciencemag.org/content/sci/348/6238/968.full>

REFERENCES

This article cites 26 articles, 1 of which you can access for free
<http://science.sciencemag.org/content/348/6238/1004#BIBL>

PERMISSIONS

<http://www.sciencemag.org/help/reprints-and-permissions>

Use of this article is subject to the [Terms of Service](#)